# Energy dependence of neutron-proton matrix element ratios derived from 25–800 MeV energy proton scattering

Norton M. Hintz, D. Cook, M. Gazzaly, and M. A. Franey
*School of Physics and Astronomy, University of Minnesota, Minneapolis, Minnesota 55455*

M. L. Barlett, G. W. Hoffmann, R. Fergerson,* J. McGill, and G. Pauletta
*Physics Department, University of Texas, Austin, Texas 78712*

R. L. Boudrie, J. B. McClelland, and K. W. Jones
*Los Alamos National Laboratory, Los Alamos, New Mexico 87545*
(Received 14 September 1987)

New data are presented on elastic and inelastic proton scattering by $^{58}$Ni at 333 and 498 MeV and $^{208}$Pb at 318 MeV. We have analyzed these data using phenomenological distorting potentials and potentials generated by folding neutron and proton densities with a free nucleon-nucleon $t$ matrix or with a medium modified nucleon-nucleon interaction. Making use of electromagnetic matrix elements, or charge transition densities, we have calculated neutron-proton transition matrix element ratios in the vibrating potential–vibrating density model ("collective form factors"), or with a scaling model in which the neutron transition densities are taken as proportional to the proton densities. In addition, we have calculated, neutron-proton matrix element ratios from earlier (p,p′) results at 25–800 MeV for $^{40}$Ca, $^{58}$Ni, and $^{208}$Pb. We conclude that, although there are some irregularities, the derived neutron/proton matrix element ratios for natural parity states show a tendency to decrease in magnitude with decreasing proton energy in the range 500–100 MeV. A quantitatively similar effect is seen in the ratio of experimental to theoretical cross sections, where the latter are calculated using transition densities adjusted to fit electron or 800 MeV proton scattering. We attribute these results to a failure of the impulse approximation and the vibrating potential model in this energy region.

## I. INTRODUCTION

In recent years, several models have been used to obtain neutron inelastic transition densities, or neutron-proton transition matrix element ratios from electron and proton scattering data at intermediate energies ($\simeq 0.1-1$ GeV).

The most naive approach is to take the (p,p′) transition potential as proportional to the derivative of the elastic optical potential [vibrating potential model (VPM)]. Inelastic cross sections are then calculated in the distorted wave Born approximation (DWBA) and normalized to data to obtain a potential deformation length, $\delta_U = \beta_U R$, where $R$ is an appropriate potential radius. A vibrating density model[1] (VDM) is then used to extract a charge deformation length, $\delta_q$ from $B(E\lambda)$ values obtained by electromagnetic methods. From $\delta_U$ and $\delta_q$, separate neutron ($\delta_n$) and proton ($\delta_p$) matter deformation lengths as well as neutron-proton transition matrix element ratios, $\tilde{M}_n/\tilde{M}_p$, can be obtained.[2] The method is expected to give meaningful results for collective states with surface-peaked transition densities.

A second, less model-dependent method is to use charge transition densities, $\rho_q(r)$, from electron scattering to calculate proton mass transition densities, $\rho_p(r)$. The neutron densities are then taken either as proportional to the proton densities [scaling model (SCM)], or to some simple surface-peaked function, such as the derivative of a two-parameter Fermi (2PF) or three parameter Gaussian (3PG) function[3,4] [semi-model-independent analysis (SMI)].

Finally, the most nearly model-independent approach (MI) is to express the neutron density in terms of a general expansion, such as the Fourier-Bessel, and to use proton densities derived, ideally, from model independent charge densities.

In the SMI and MI analyses, searches are made on the neutron density parameters to best fit the data. The proton inelastic transition amplitude can be calculated in the distorted wave impulse approximation (DWIA) using the free nucleon nucleon (N-N) interaction, or in the distorted wave Born approximation (DWBA) using phenomenological effective forces or theoretical medium modified forces.

In most of the VPM analyses, the elastic optical potentials have been purely phenomenological (POP). However, in the SMI and MI analysis the distorting potential is usually calculated by folding the ground state neutron and proton static densities with the same interaction as is used in the inelastic calculation ("consistent model").

In this paper, we present new data on $^{208}$Pb(p,p′) at 318 MeV, and on $^{58}$Ni(p,p′) at 333 and 498 MeV. We will discuss the results of VPM-VDM and SCM analysis

 

of this data and compare these with results derived from other work in the 100–800 MeV region on these nuclei and on $^{40}$Ca. Some results from the analysis of low energy ( $<100$ MeV) data are also included for comparison.

In presenting the final results, we choose to display the reduced neutron-proton matrix element ratios, $\tilde{M}_n/\tilde{M}_p$, where we define

$$\tilde{M}_i(\lambda)=\frac{1}{N \text{ or } Z}\int_0^\infty \rho_i(r)r^{\lambda+2}dr \ . \quad (1)$$

The quantity $\rho_i(r)$ is either the point proton (p), point neutron (n), or charge ($q$) transition density. The $B(E\lambda)\uparrow$ from a spin zero ground state is given in our convention by

$$B(E\lambda)\uparrow = |\, Z\tilde{M}_q(\lambda)\,|^2 \ . \quad (2)$$

In these analyses we are neglecting contributions from spin and current densities which are known to be small for the low lying collective states discussed here. Also, although the (p,p') transition amplitudes cannot be expressed in terms of the matrix elements $M_i(\lambda)$, once the transition densities $\rho_i(r)$ have been determined (in some model), the $M_i(\lambda)$ can be calculated. The fact that different probes will sample different regions of $\rho_i(r)$ will of course lead to errors in the derived $M_i(\lambda)$ if the true $\rho_i(r)$ have not been determined.

The main conclusion of this paper is that, despite some irregularities, a significant bombarding energy dependence appears below about 500 MeV in the $\tilde{M}_n/\tilde{M}_p$ ratios derived by most of the methods above. Thus, we believe that this is not a property of the model used for $\rho_i(r)$, but a deficiency in the transition potential in this region, derived either from phenomenological optical potentials (VPM) or from folding models in which free or effective N-N interactions are used (SCM, SMI, and MI analyses).

## II. EXPERIMENT

The $^{208}$Pb(p,p') data at 318 MeV were taken with the High Resolution Spectrometer Facility (HRS) at the Los Alamos Clinton P. Anderson Meson Physics Facility (LAMPF). Enriched ($>98\%$) $^{208}$Pb targets of

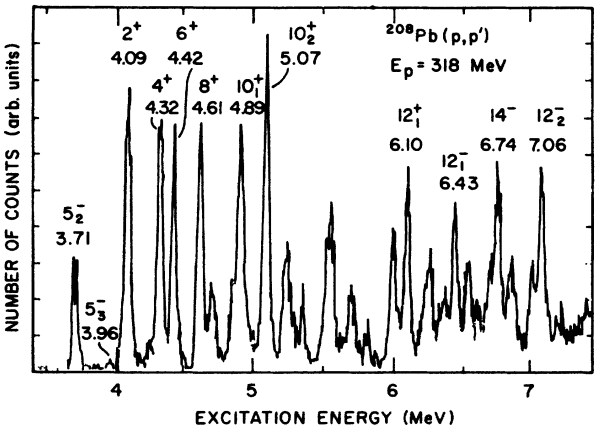


FIG. 1. Spectrum of $^{208}$Pb(p,p') at $T_p=318$ MeV, $\theta_{lab}=28°$.

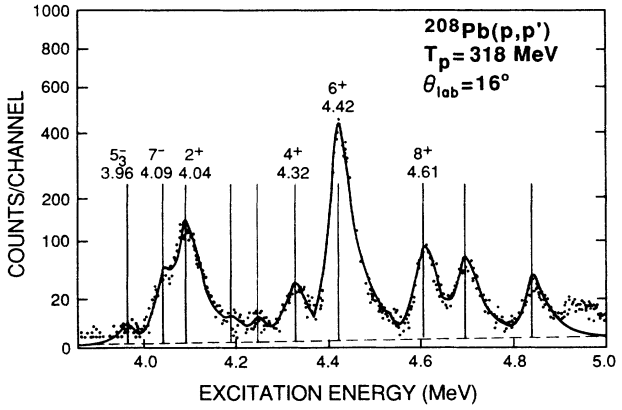


FIG. 2. Spectrum of $^{208}$Pb(p,p') at $T_p=318$ MeV, $\theta_{lab}=16°$ showing peak fitting by program LOAF. (Quadratic ordinate.)

$\rho x \simeq 20$–$25$ mg/cm$^2$ were used. Experimental details can be found in a number of earlier papers.[5,6] The overall energy resolution full width at half maximum (FWHM) was generally in the vicinity of $\Delta E \simeq 40$ KeV. Absolute cross sections were obtained by normalizing to known p + p elastic cross sections.[7] This method is believed to produce absolute normalizations to 10% or better. An independent measurement of the $^{208}$Pb+p elastic cross section at 334 MeV by Bertrand, *et al.*[8] is in agreement with our normalization to better than 5%. The spectra were stripped using the program LOAF.[9] The $3_1^-$ ( 2.61 MeV), $5_1^-$ (3.20), and $5_2^-$ (3.71) states were clearly resolved. However the $5_3^-$ (3.96), $7^-$ (4.04), $2_1^+$ (4.09), $4_1^+$ (4.32), $6_1^+$ (4.42) and $8_1^+$ (4.61) states are known to have weakly excited neighbors within our line width.[10] No evidence was seen for the excitation of these neighboring states in peak centroid shifts with angle, or in the angular distributions. A spectrum at $\theta_L=28°$ and a sample of peak fitting are shown in Figs. 1 and 2. Data were also obtained on high spin states ($J=10-14$) in the 5–7 MeV region but these have been discussed in an earlier paper.[6]

Elastic and inelastic proton cross sections were also measured for $^{58}$Ni at $T_p=333$ and 498 MeV in earlier experiments. Details of the experiments and their results for the $6_1^+$ (5.13 MeV) state have been published.[5]

The cross sections for the ground and low-lying states of $^{208}$Pb and $^{58}$Ni are shown in Figs. 3–14.

## III. ANALYSIS

### A. Vibrating potential model (VPM)

#### 1. $^{208}$Pb

The low lying states of $^{208}$Pb were first analyzed with the simple VPM to obtain potential deformation lengths, $\delta_U=\beta_U R$. The elastic cross section data from this experiment at 318 MeV, and analyzing power ( $A_y$ ) data at 300 MeV,[11] were fit using the search program RELOM (Ref. 12) with a 2PF optical potential which included spin-orbit terms. The 300 MeV data were "converted"

TABLE I. Phenomenological optical potential[a] parameters[b] for $^{208}$Pb at 318 MeV.

| Central | $V$ | $r_v$ | $a_v$ | $V_z$ | $r_z$ | $a_z$ | $W$ | $r_w$ | $a_w$ |
|---|---|---|---|---|---|---|---|---|---|
| POP-I | −5.88 | 1.306 | 0.552 | 0 | | | −27.04 | 1.156 | 0.664 |
| POP-II | −9.80 | 1.33 | 0.63 | 11.95 | 0.87 | 0.95 | −26.23 | 1.13 | 0.71 |

| Spin-orbit | $V_{so}$ | $r_{so}$ | $a_{so}$ | $W_{so}$ | $r_c$ |
|---|---|---|---|---|---|
| POP-I | −1.75 | 1.07 | 0.640 | 2.73 | 1.05 |
| POP-II | −2.41 | 1.10 | 0.70 | 0.97 | 1.05 |

[a]The potentials were of the form

$$U(r)=Vf(r,r_v,a_v)-4a_zV_z\frac{d}{dr}f(r,r_z,a_z)+iWf(r,r_w,a_w)-(V_{so}+iW_{so})\frac{2}{r}\frac{d}{dr}f(r,r_{so},a_{so})\boldsymbol{l}\cdot\boldsymbol{\sigma}\ ,$$

where $f(r,r_x,a_x)=[1+\exp(r-R_x)/a_x]^{-1}$,

$$R_x=r_xA^{1/3}\ .$$

[b]Potentials are in MeV, lengths in fm.

to 318 MeV using momentum transfer as the common variable. The resulting phenomenological optical potential parameters (POP-I) are given in Table I. The predicted elastic cross section, shown as a solid line in Fig. 3, is not completely satisfactory, with a $\chi^2/N=40$ in contrast to the situation at 800 MeV (Ref. 2) where an excellent fit was obtained with a 2PF potential. An attempt was made to obtain a better fit to the cross section and analyzing power data by using the sum of a 2PF and the derivative of a 2PF function whose parameters are given in Table I. This potential (POP-II) gave a shape having a surface oscillation in the real central potential, similar to that obtained from folding the Geramb medium corrected interaction[6,13] with the best available neutron and proton ground state densities. The resulting improved $\chi^2$ per point was $\chi^2/N=15$ for the fit shown as a dashed line in Fig. 3.

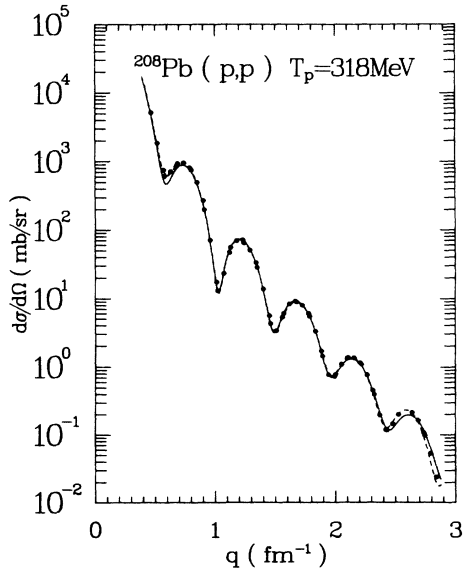


FIG. 3. Differential elastic cross section for $^{208}$Pb(p,p) at $T_p=318$ MeV. Solid (dashed) line shows optical model predictions for POP-I (POP-II) of Table I.

Inelastic cross sections were then calculated by "deforming" the optical potentials, including the spin-orbit terms. Generally the three deformation parameters, $B_v$, $B_w$, $B_{so}$ were set equal (then $B_c\equiv B_v=B_w$). For the low spin states ($J\leq 5$) the best fits were obtained with $\beta_c=\beta_{so}$, but for $J\geq 6$, $\beta_{so}>\beta_c$ was favored as was noted also at 135 MeV.[14] The resulting angular distributions for $^{208}$Pb normalized to the data at forward angles to obtain $\beta_U^2$ are shown in Figs. 4 and 5 for the 2PF potential (POP-I). The simple VPM predictions do not agree with the data as well as they did at 800 MeV.[2]

When the POP-II potential was deformed, according to the VPM prescription, the shape of the inelastic cross sections was poorly reproduced. However, the deformation lengths, obtained by normalizing to the data at the

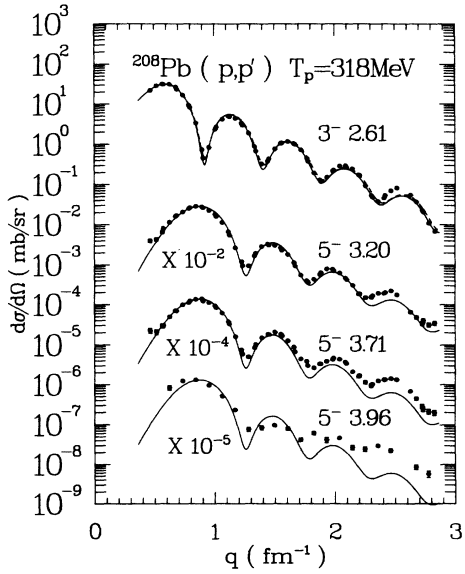


FIG. 4. Inelastic cross sections for $^{208}$Pb(p,p') at $T_p=318$ MeV for $3_1^-$, $5_1^-$, $5_2^-$, and $5_3^-$ states. Energies are shown in MeV. Solid curves show predictions of VPM ("collective form factors") with POP-I and $\beta_{so}=\beta_c$. Dashed curve is for $\beta_{so}=1.1\beta_c$.

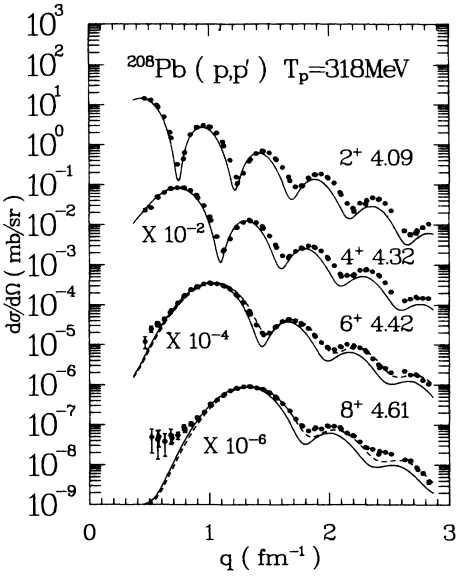


FIG. 5. Same as Fig. 4 but for $2_1^+$, $4_1^+$, $6_1^+$, and $8_1^+$ states. Dashed curve is for $\beta_{so}=1.5\beta_c$.

first maximum, are very close to those obtained with the POP-I.

Since the real and imaginary radii ($R_v$,$R_w$) are not, in general, equal, some weighted average radius, $\bar{R}$, must be chosen to calculate deformation lengths, $\delta_U=\beta_U\bar{R}$. If it is assumed that the real and imaginary cross sections at small angles are proportional to the volume integrals of the corresponding potentials, the appropriate $\bar{R}$ is given by (see Appendix),

$$\bar{R}=\left[\frac{(VR_v^3)^2+(WR_w^3)^2}{(VR_v^2)^2+(WR_w^2)^2}\right]^{1/2}. \tag{3}$$

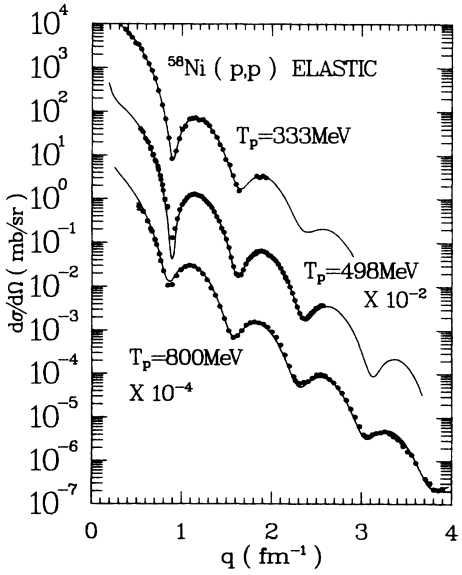


FIG. 6. Elastic cross sections for $^{58}$Ni(p,p) at $T_p=333$, 500, and 800 MeV. Solid curves are optical model predictions with parameter sets $P2(333)$, $P3(500)$, and $MK(800)$ given in Table III.

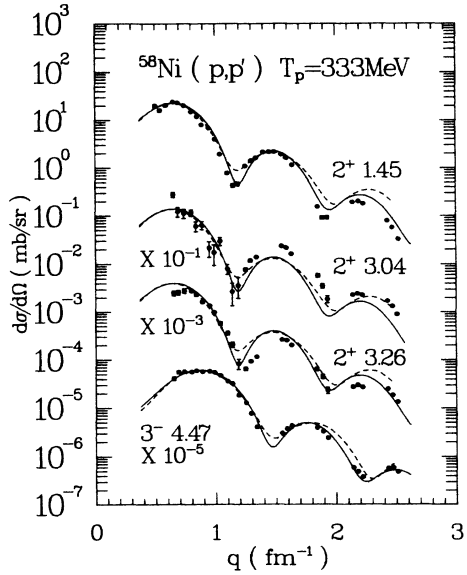


FIG. 7. Inelastic scattering cross sections for $^{58}$Ni(p,p') at $T_p=333$ MeV for $2_1^+$ (1.45), $2_3^+$ (3.04), $2_4^+$ (3.26), and $3_1^-$ (4.47 MeV) states. Solid (dashed) curves are VPM predictions with $P2(SN)$ potentials of Table III, and $\beta_{so}=\beta_c$.

The values of $\delta_U$ so calculated are displayed in Table II along with those at other energies calculated using the $\bar{R}$ of Eq. (3), with the parameters given by the various authors. It should be mentioned that in the analysis of the low energy ($T_p<100$ MeV) data the authors have used surface absorption terms in the optical potential, and so to the extent that these contribute to the inelastic cross sections the results are not strictly comparable to the analyses above 100 MeV where only volume absorption terms were used. It can be seen that, despite some fluctuations, there seems to be a systematic increase in $\delta_U$ with increasing proton energy above about 100 MeV.

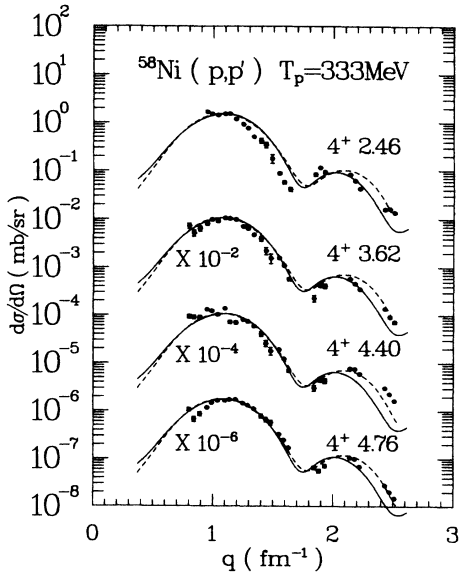


FIG. 8. Same as Fig. 7 for $4^+$ states at $E_x=2.46$, 3.62, 4.40, and 4.76 MeV.

TABLE II. Potential deformation lengths[a] $\delta_u = \beta_u \bar{R}$, from VPM analysis of $^{208}$Pb(p,p′) data at various incident energies.

| $J^\pi$ ($E_x$ MeV) | 35 MeV[b] | 61 MeV[c] | 65 MeV[d] | 80 MeV[e] | 98 MeV[e] | 120 MeV[e] | 135 MeV[f] | 155 MeV[g] | 200 MeV[h] | 318 MeV[i] | 334 MeV[h] | 400 MeV[h] | 800 MeV[j] | 800 MeV[k] |
|---|---|---|---|---|---|---|---|---|---|---|---|---|---|---|
| $3_1^-$ (2.61) | 0.833 | 0.745 | 0.83 | 0.67 | 0.73 | 0.64 | 0.729 | 0.75 | 0.75 | 0.763 | 0.83 | 0.80 | 0.825 | 0.803 |
| $5_1^-$ (3.20) | 0.403 | 0.318 | | | | | 0.313 | | 0.35 | 0.342 | | 0.35 | 0.401 | 0.390 |
| $5_2^-$ (3.71) | 0.236 | 0.232 | | | | | 0.219[l] | | 0.22 | 0.238 | | 0.23 | 0.283 | 0.276 |
| $5_3^-$ (3.96) | (0.125) | | | | | | | | | (0.0733) | | | | |
| $2_1^+$ (4.09) | 0.403 | 0.398 | 0.37 | | 0.345 | | 0.401 | 0.370 | 0.39 | 0.393 | 0.416 | 0.42 | 0.466 | 0.464 |
| $4_1^+$ (4.32) | 0.465 | 0.463 | | | | | 0.466 | | 0.48 | 0.495 | 0.478 | 0.56 | 0.546 | 0.537 |
| $6_1^+$ (4.42) | 0.431 | 0.413 | | | | | | | | 0.445 | | | 0.514 | 0.504 |
| | | | | | | | 0.379[l] | | | 0.394[l] | | | | |
| $8_1^+$ (4.61) | 0.278 | 0.290 | | | | | | | | 0.281 | | | 0.359 | 0.344 |
| | | | | | | | 0.138[m] | | | 0.237[l] | | | | |
| $\bar{R}$ (fm) | 6.943 | 7.237 | 7.225 | 7.263 | 7.355 | 7.456 | 7.287 | 7.121 | $\delta_v = \delta_w$ | 6.917 | $\delta_v = \delta_w$ | $\delta_v = \delta_w$ | 6.203 | 6.475 |
| $G^n$ | [o] | [o] | [o] | [o] | 0.122 | [o] | 0.122 | [o] | 1.46 | 2.32 | 2.10 | 457 | 2.53 | 0.130 |

[a] $\beta_c = \beta_{so}$ unless noted. When $\beta_c \neq \beta_{so}, \beta_U = \beta_c$. $\bar{R}$ is from Eq. (3).
[b] From Ref. 26.
[c] Reference 27.
[d] Reference 28.
[e] Reference 29. For $\bar{R}$ we used average of our $\bar{R}$ [Eq. (3)] and $R_{opt}$ of Reference 29 for $3^-$ state. $\delta_u$ for $2_1^+$ state has been renormalized by ratio of new to old values for $3^-$ state given in Ref. 29.
[f] Reference 14.
[g] References 30 and 31.
[h] References 8, 32 and 34.
[i] This work, POP-I from Table I
[j] From Ref. 2, spin-orbit couplings omitted in elastic and inelastic channels.
[k] Phenomenological optical potential including spin-orbit terms, spin-orbit coupling included in inelastic channel: $V = 20.3$, $r_v = 1.054$, $a_v = 0.497$, $w = -65.6$, $r_w = 1.096$, $a_w = 0.639$, $v_{so} = -0.674$, $w_{so} = -0.151$, $r_{so} = 1.148$, $a_{so} = 0.733$, $r_c = 1.05$ (all MeV, fm). Potential defined in footnote [a], Table I.
[l] $\beta_{so} = 1.5\beta_c$.
[m] $\beta_{so} = 2.5\beta_c$.
[n] Value of $G$ used in Eqs. (A16).
[o] Linear Eq. (A17) used.

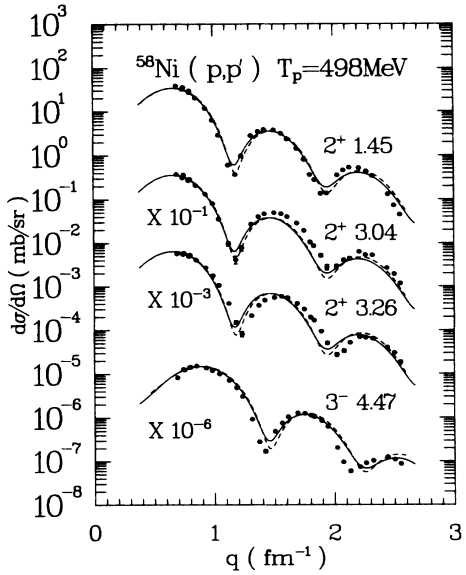


FIG. 9. Inelastic scattering cross sections for $^{58}$Ni(p,p') at $T_p=498$ MeV for $2^+$ states at 1.45, 3.04, 3.26 MeV and $3^-$ state at 4.47 MeV. Solid (dashed) curves are VPM predictions with $P3(SN)$ potentials of Table III and $\beta_{so}=\beta_c$.

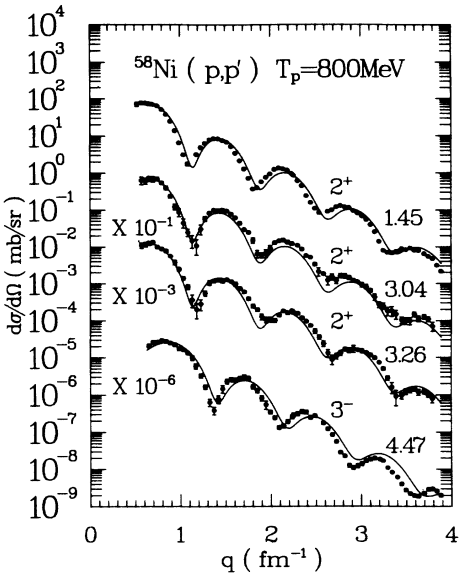


FIG. 11. Inelastic cross sections for $^{58}$Ni(p,p') at $T_p=800$ MeV for $2^+$ states at 1.45, 3.04, 3.26 MeV and $3^-$ state at 4.47 MeV. Solid curves are VPM predictions with $MK$ potential of Table III, and $\beta_{so}=\beta_c$. The data are from Ref. 15.

In Sec. IV we will show that this is reflected in a systematic increase in the derived values of $\tilde{M}_n/\tilde{M}_p$ with increasing bombarding energy.

### 2. $^{58}$Ni

The VPM was also used, as described above, to obtain potential deformation lengths, $\delta_U$, from the $^{58}$Ni(p,p') data at $T_p=333$ and 498 MeV. Data from an earlier experiment at 800 MeV (Ref. 15) were reanalyzed with the inclusion of the spin-orbit terms in the transition potential. New optical potential searches were made at all three energies using elastic cross section and, if available, $A_y$ data. (None of the latter exists at 333 MeV.) The resulting new potentials ($P1$, $P2$, $P3$ and $MK$) are given in Table III, along with earlier sets ($SN$ and $K1$) from Refs. 5 and 15. At 333 MeV the $P1$ and $P2$ potentials are not significantly better than the original $SN$ potential, none being completely satisfactory. The $P1$ and $P2$ potentials give similar deformation lengths, both slightly lower than the $SN$ potential. At 500 and 800 MeV, the new potentials ($P3$ and $MK$) are somewhat better than the older $SN$ and $K1$ sets. All sets, given in Table III, give comparable fits to the inelastic cross sections. The elastic cross sections are shown in Fig. 6 and the inelastic in Figs. 7–12, along with the theoretical predictions. The deformation lengths, $\delta_U$, obtained by normalizing

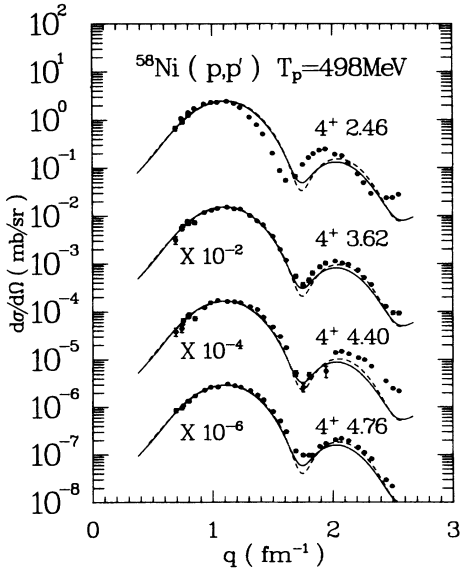


FIG. 10. Same as Fig. 9 except for $4^+$ states at 2.46, 3.62, 4.40, and 4.76 MeV.

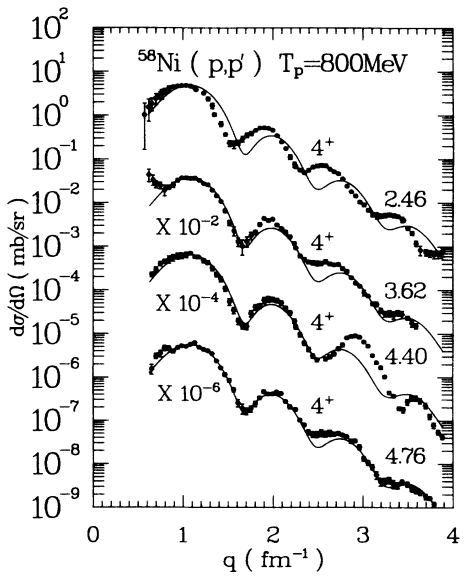


FIG. 12. Same at Fig. 11 except for $4^+$ states at 2.46, 3.62, 4.40, and 4.76 MeV.

TABLE III. Optical model parameters[a] for $^{58}$Ni+p at various energies.

| $T_p$ (MeV) | Potential set | $V$ | $r_v$ | $a_v$ | $W$ | $r_w$ | $a_w$ | $V_{so}$ | $W_{so}$ | $r_{so}$ | $a_{so}$ | $r_c$ |
|---|---|---|---|---|---|---|---|---|---|---|---|---|
| 333 | $SN$[b] | −10.3 | 1.307 | 0.572 | −42.5 | 1.016 | 0.554 | −0.700 | 1.21 | 1.093 | 0.444 | 1.20 |
| | $P1$ | −9.53 | 1.139 | 0.584 | −85.5 | 0.847 | 0.656 | −1.22 | 0.905 | 1.149 | 0.608 | 1.20 |
| | $P2$ | −39.0 | 0.926 | 0.604 | −50.4 | 0.880 | 0.780 | −1.21 | 1.53 | 1.099 | 0.675 | 1.20 |
| 498 | $SN$[b] | −9.27 | 1.227 | 0.582 | −60.5 | 0.984 | 0.598 | −0.349 | 2.59 | 1.022 | 0.657 | 1.05 |
| | $P3$ | −6.85 | 1.321 | 0.492 | −49.0 | 1.034 | 0.628 | −0.981 | 4.39 | 0.981 | 0.681 | 1.20 |
| 800 | $MK$ | 24.1 | 0.934 | 0.518 | −79.0 | 1.005 | 0.598 | −1.137 | −0.180 | 0.970 | 0.805 | 1.05 |
| | $K1$[c] | 6.3 | 0.977 | 0.689 | −64.2 | 1.047 | 0.580 | −1.16 | −2.52 | 0.955 | 0.767 | 1.17 |

[a]Potentials are of the form given in Table I footnote: Energies are in MeV, lengths in fermis.
[b]Potential from Ref. 5.
[c]Potential 1 from Ref. 15.

TABLE IV. Deformation lengths, $\delta_U = \beta_U \bar{R}$ from VPM analysis of $^{58}$Ni(p,p′) at various proton energies and for several potential sets.[a] Shown also are proton deformation lengths.[b]

| | | 333 MeV | | 498 MeV | | 800 MeV[c] | |
|---|---|---|---|---|---|---|---|
| $J^\pi$ ($E_{x_1}$ MeV) | $\delta_p$[b] | $SN$ | $P2$ | $SN$ | $P3$ | $MK$ | $K1$[d] |
| $2^+$ (1.45) | 0.821 | 0.832 | 0.804 | 0.812 | 0.806 | 0.878 | 0.902 |
| $2^+$ (3.04) | 0.280 | 0.206 | 0.199 | 0.264 | 0.261 | 0.278 | 0.270 |
| $2^+$ (3.26) | 0.354 | 0.351 | 0.339 | 0.354 | 0.350 | 0.361 | 0.37 |
| $3^-$ (4.48) | 0.828 | 0.606 | 0.573 | 0.730 | 0.704 | 0.728 | 0.778 |
| $4^+$ (2.46) | 0.396 | 0.386 | 0.356 | 0.374 | 0.351 | 0.404 | 0.403 |
| $4^+$ (3.62) | 0.441 | 0.323 | 0.299 | 0.296 | 0.277 | 0.354 | 0.36 |
| $4^+$ (4.40) | 0.378 | 0.323 | 0.298 | 0.308 | 0.288 | 0.471 | 0.47 |
| $4^+$ (4.76) | 0.441 | 0.418 | 0.386 | 0.410 | 0.384 | 0.436 | 0.42 |
| $\bar{R}$ | | 4.108 | 3.483 | 3.866 | 4.066 | 3.874 | 4.053 |
| $G$[e] | | 1.39 | 0.381 | 0.416 | 0.506 | 0.0627 | |

[a]Optical potentials given in Table III, $\bar{R}$ from Eq. (3).
[b]Calculated, from weighted average of $B(E\lambda)$ values given in Refs. 2 and 40, using Eqs. (7) and (8).
[c]Data from Ref. 15.
[d]Analysis of Ref. 15, spin orbit coupling in elastic channel only, $\bar{R} = R_w$.
[e]Value of $G$ used in Eqs. (A16).

TABLE V. Scaling model (SCM) parameters, $\alpha$[a], for various optical potentials and N-N interactions for $^{208}$Pb(p,p′) at 318 and 800 MeV.

| | | | $T_p = 318$ MeV | | | $T_p = 800$ MeV | |
|---|---|---|---|---|---|---|---|
| Optical potential ground state density | POP-I | POP-II | Folded Refs. 19 and 20 $+\rho^2$ term | Folded Refs. 19 and 20 | Folded p: Ref. 19 n: varied | POP[c] | POP[d] |
| N-N interaction[b] | LF | LF | LF | von Geramb | von Geramb | LF | LF |
| state, $J^\pi$ ($E_x$, MeV) | | | | | | | |
| $3_1^-$ (2.61) | 0.86 | 0.84 | 0.80 | 1.02 | 0.91 | 1.09 | 1.14 |
| $5_1^-$ (3.20) | 1.02 | 0.98 | 0.94 | 1.16 | 1.04 | 1.28 | 1.32 |
| $5_2^-$ (3.71) | 0.85 | 0.81 | 0.78 | 0.98 | 0.87 | 1.11 | 1.14 |
| $2_1^+$ (4.09) | 0.80 | 0.78 | 0.77 | 1.02 | 0.91 | 1.31 | 1.37 |
| $4_1^+$ (4.32) | 0.83 | 0.79 | 0.76 | 1.01 | 0.89 | 1.15 | 1.18 |
| $6_1^+$ (4.42) | 0.82 | 0.76 | 0.72 | 0.96 | 0.84 | 1.06 | 1.09 |
| $8_1^+$ (4.61) | 0.95 | 0.89 | 0.81 | 1.07 | 0.92 | 1.33 | 1.37 |

[a]$\rho_n^{tr} = \alpha N/Z\rho_p^{tr}$, $\rho_p^{tr}$ derived from Ref. 16 data.
[b]Nucleon-nucleon interaction used in generating transition potential and optical potential if derived from folding. LF force is from Ref. 17, von Geramb force from Ref. 13.
[c]Phenomenological potential from Ref. 2. Spin orbit potential omitted.
[d]Phenomenological optical potential including spin-orbit terms, given in footnote k, Table II.

theory to experiment at the first maxima are given in Table IV. The pattern shown by the $\delta_U$ as a function of energy is somewhat irregular, but the averages of the 333 and 500 MeV values are significantly lower than those at 800 MeV.

### B. Scaling model (SCM) analysis.

We have also analyzed the 318 MeV and 800 MeV $^{208}$Pb(p,p′) data with the scaling model (SCM), assuming for the neutron transition density,

$$\rho_n(r)=\alpha\rho_p(r)N/Z \ . \tag{4}$$

Thus for the scaling model, $\tilde{M}_n/\tilde{M}_p=\alpha$.

The proton transition densities, $\rho_p(r)$, were obtained by unfolding nucleon charge distributions from the charge densities of Heisenberg, *et al.*[16]. Cross sections were calculated in the DWIA using the Love-Franey[17] (LF) interaction. The scaling parameter, $\alpha$, was adjusted to give the best normalization of theory to the data. The results for $T_p=318$ MeV, using the phenomenological optical potentials of Table I to model the distortion, are shown in Figs. 13 and 14. The values of $\alpha$ obtained are given in Table V.

In the original SCM analysis of the $^{208}$Pb(p,p′) data at 800 MeV, a phenomenological optical potential (POP) without a spin-orbit term was used. In addition, an earlier version of the LF force was used. We repeated the 800 MeV analysis with a new POP, including a spin-orbit term, and using the most recent LF force.[17] The predicted elastic and inelastic cross sections are shown in Figs. 15–17. The results for $\alpha$, shown in the last column of Table V, are very close to the original values shown in the next to last column.

It can be seen that the derived values of $\alpha$ at 318 MeV are all lower than those at 800 Mev. This effect is the same qualitatively (and quantitatively as we shall show later) as the energy dependence of the deformation lengths shown in Table II.

Several additional optical potential and N-N force options were tried for $^{208}$Pb at 318 MeV in the scaling model. These included the following.

(1) The use of the von Geramb[13] or GBJ (Ref. 18) medium corrected interactions ("*G*-matrix ") rather than the free LF "*t* matrix" to calculate the transition amplitudes and/or to derive the optical potential by folding.

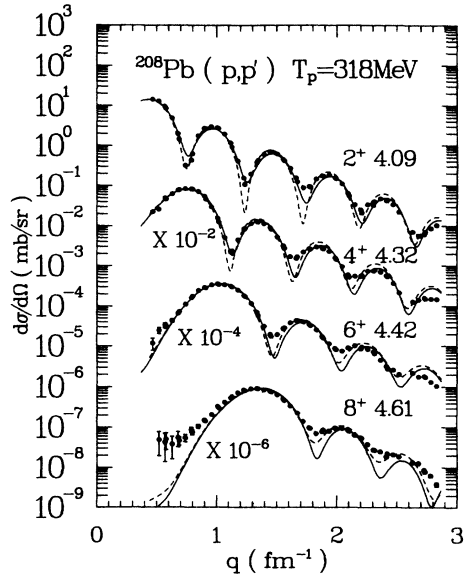


FIG. 14. Same as for Fig. 13 except for $2_1^+$, $4_1^+$, $6_1^+$, and $8_1^+$ states.

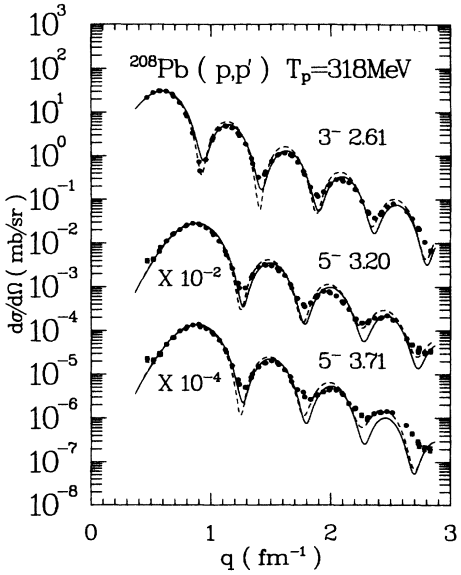


FIG. 13. Inelastic cross sections for $^{208}$Pb(p,p′) at $T_p=318$ MeV for $3_1^-$, $5_1^-$, and $5_2^-$ states. Solid (dashed) curves show scaling model (SCM) predictions with LF interaction using POP-I (POP-II) potentials of Table I as described in text, Sec. III B. Excitation energies are shown in MeV.

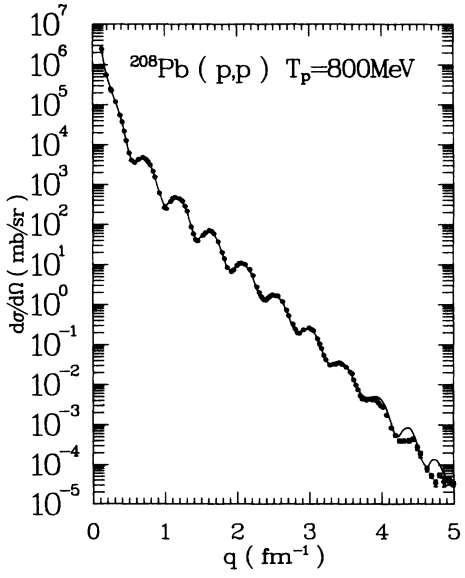


FIG. 15. Differential elastic cross sections for $^{208}$Pb(p,p) at $T_p=800$ MeV. The solid curve shows prediction based on phenomenological optical potential including spin-orbit terms. The potential parameters are given in the Table II footnote k. The data are from Ref. 2.

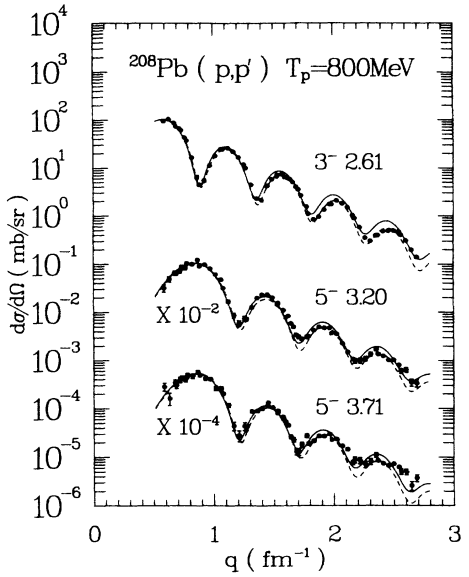


FIG. 16. Inelastic cross sections for $^{208}$Pb(p,p') at $T_p=800$ MeV for $3_1^-$, $5_1^-$, and $5_2^-$ states (energies in MeV). Solid and dashed curves show SCM predictions with the LF interaction. The dashed curve was calculated using the distorting potential of Ref. 2 (Set II), without spin-orbit terms. The solid curve is based on an optical potential which includes a spin orbit term. The potential parameters for the later are given in the Table II footnote. The data are from Ref. 2.

(2) The addition of phenomenological $\rho^2$ terms to the ground state isoscalar densities to improve the elastic fits obtained with optical potentials generated by folding (first order *KMT*). The $\rho^2$ terms simulate quadratic terms which arise in second order *KMT* and in Dirac relativistic theories.

(3) The use of alternate ground state neutron densities. In most of the folding calculations (to generate the optical potential) the ground state proton point density

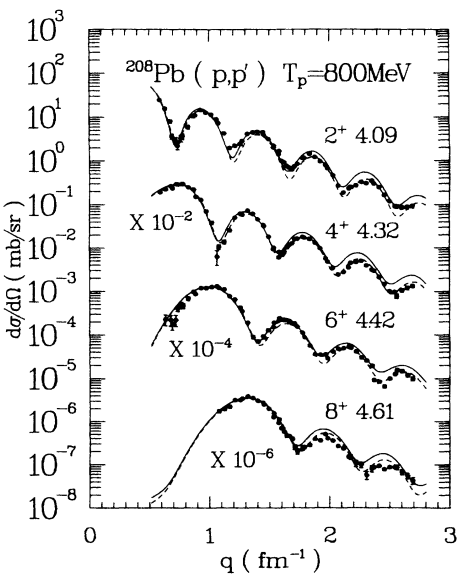


FIG. 17. Same as Fig. 15 except for $2_1^+$, $4_1^+$, $6_1^+$, and $8_1^+$ states.

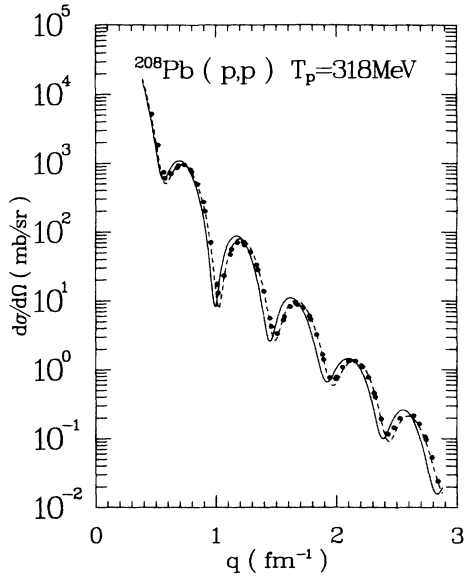


FIG. 18. Differential elastic cross section for $^{208}$Pb(p,p) at $T_p=318$ MeV. The curves show predictions based on potentials generated by folding the von Geramb force (Ref. 13) with neutron and proton densities. For the solid curve the densities were taken from experiment (Refs. 19 and 20); for the dashed curve the proton density was from Ref. 19, but the neutron density was adjusted to fit the data.

was derived from the electron scattering charge density[19] and the neutron density was taken from an 800 MeV (p,p') second order *KMT* analysis.[20] However, in some of the calculations the ground state neutron density was parameterized (2PG or 3PG) and allowed to vary to obtain the best agreement with the elastic data. Although a fairly good fit was obtained in this last procedure, the

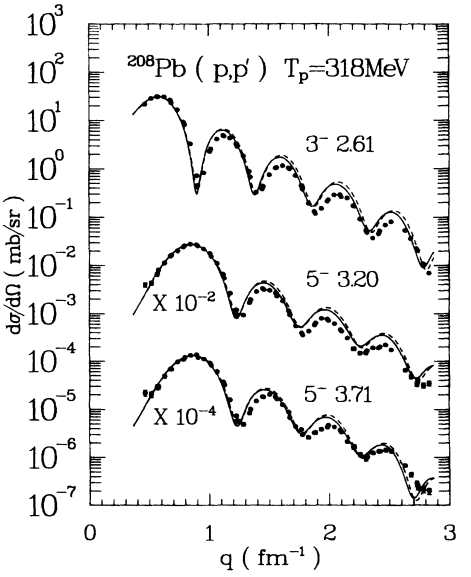


FIG. 19. Inelastic cross sections for $^{208}$Pb(p,p') at $T_p=318$ MeV to $3_1^-$, $5_1^-$, and $5_2^-$ states. Energies are given in MeV. The solid (dashed) curve shows SCM predictions based on the von Geramb force and experimental (neutron adjusted) densities to obtain the distorting potential as described in the Fig. 18 caption.

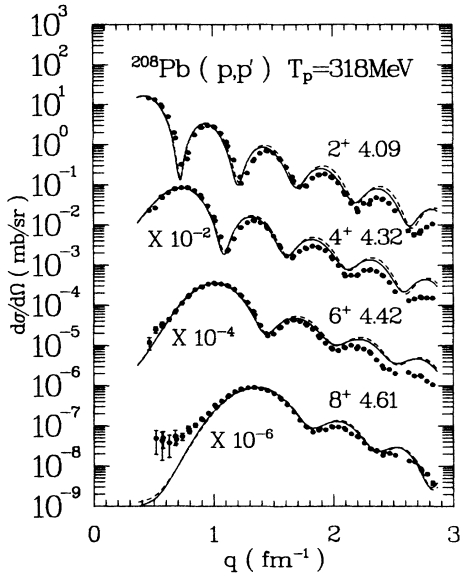


FIG. 20. Same as Fig. 19 except for $2_1^+$, $4_1^+$, $6_1^+$, and $8_1^+$ states.

value of $\Delta r_{np} = \langle r_n^2 \rangle^{1/2} - \langle r_p^2 \rangle^{1/2}$ resulting was found to be $\Delta r_{np} \simeq -0.20$, in disagreement with the accepted value of $\Delta r_{np} \simeq +(0.1 \text{ to } 0.2)$.

Not all combinations of the above models were tried, but the resulting scaling parameters for some representative sets are shown in Table V and the cross sections in Figs. 18–20. Again, it is seen that although there is some variation in the $\alpha$ values derived with the various models at 318 MeV, they are all systematically lower by $\simeq 30\%$ than those at 800 MeV. The set giving values closest to the 800 MeV values, which we believe to be the most nearly correct, is the one using a folded optical potential, with the von Geramb force[13] used to generate both the optical and transition potentials. However this set (option 1 above), and the option 3 procedure gave the poorest representations of the inelastic data. A more complete discussion of the VPM and SCM analyses of the 318 MeV, $^{208}$Pb(p,p') data are given elsewhere.[21]

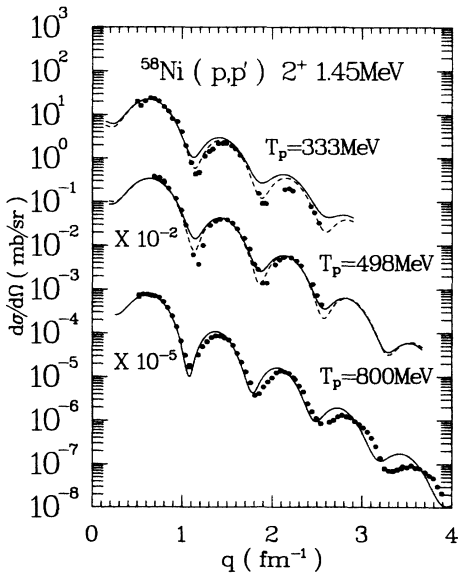


FIG. 21. Inelastic cross sections for $^{58}$Ni(p,p') for $2_1^+$ (1.45 MeV) state at $T_p = 333$, 498, and 800 MeV. The 800 MeV data are from Ref. 15. The curves show SCM predictions based on the proton transition density from Ref. 16. The phenomenological optical potentials for the solid (dashed) curves are *P2(SN)* at 333 MeV, *P3(SN)* at 498 MeV, and *MK* at 800 MeV. The potential parameters are given in Table III.

Scaling Model (SCM) calculations were also done for the $2_1^+$ (1.45 MeV) state of $^{58}$Ni at $T_p = 333$, 500, and 800 MeV. (The 800 MeV data are from Ref. 15). The proton transition density was obtained from Ref. 16. The predicted cross sections are shown, with the data, in Fig. 21 for several optical potentials. The values of $\alpha$ obtained are given in Table VII ($\alpha = \tilde{M}_n/\tilde{M}_p$ in the SCM).

### C. Model independent (MI) and semi-model-independent (SMI) analyses

To date only one model independent analysis, to obtain neutron transition densities from inelastic proton (and electron) scattering data at intermediate energies, has been published. Kelly, *et al.*[22] have derived a neutron transition density for the $2_1^+$ state of $^{18}$O using a proton density derived from electron scattering and a polynomial times Gaussian expansion for the neutron density. The Geramb medium modified force,[13] based on the Paris potential, was used to calculate the distorted waves and inelastic transition amplitude to compare with the data at $T_p = 135$ MeV. It is interesting to note that it was necessary to multiply the resultant calculations by 0.74 to fit the $2_1^+$ state of $^{16}$O, which was used for calibration (since here $\rho_n = \rho_p$). The same factor was then applied to the $^{18}$O ($2_1^+$) calculation. This factor is similar to the renormalization factors we find at 318 MeV to give agreement with $\tilde{M}_n/\tilde{M}_p$ ratios determined at 800 MeV (Table V).

Semi-model-independent (SMI) analyses have been done of 800 and 500 MeV (p,p') data on $^{208}$Pb($3^-$,$5^-$) and $^{40}$Ca($2^+$,$3^-$) by Ray and Hoffman[3] and by Barlett, Hoffman, and Ray[4] in which proton densities were obtained from (e,e') (Ref. 16) and neutron densities were represented by surface peaked two parameter Fermi (2PF) or three parameter Gaussian (3PG) functions. In the 800 MeV analysis[3] the distorting optical potential was generated in second order *KMT* and the inelastic cross sections then calculated in the DWIA. For both, the free N-N amplitudes of Arndt[23] (solution SM 80) were used. The parameters of the neutron transition density were then adjusted to best reproduce experiment. No significant differences in the quality of fit were found for the 2PF and 3PG neutron densities.

In the 500 MeV analysis,[4] the same procedures were used except that a phenomenological effective N-N force was employed in both the elastic and inelastic channels. The isoscalar effective force was obtained by fitting the 500 MeV *elastic* cross section, analyzing power and spin rotation ($Q$) data on $^{40}$Ca in a first order *KMT* ("$t\rho$") approximation.[24] Densities for $^{40}$Ca were derived from charge densities with a small theoretical correction for the neutron-proton difference. The small isovector part

TABLE VI. Reduced neutron-proton matrix element ratios, $\tilde{M}_n/\tilde{M}_p$ for $^{208}$Pb derived by various methods.

| Method[a] | $T_p$ (MeV) | State, $J^\pi$ $3_1^-$ | $5_1^-$ | $5_2^-$ | $2_1^+$ | $4_1^+$ | $6_1^+$ | $8_1^+$ | References,[b] comments |
|---|---|---|---|---|---|---|---|---|---|
| VPM-VDM | 800 | 1.12 | 1.18 | 1.10 | 1.28 | 1.10 | 0.79 | 1.87 | Ref. 2, no s-o |
| VPM-VDM | | 1.07 | 1.12 | 1.07 | 1.25 | 1.07 | 0.79 | 1.70 | This, with s-o[c] |
| SCM | | 1.09 | 1.28 | 1.11 | 1.31 | 1.15 | 1.06 | 1.33 | Table V, Next to last column |
| | | 1.14 | 1.32 | 1.14 | 1.37 | 1.18 | 1.09 | 1.37 | Table V, last column |
| SMI | | 1.12 | | | | | | | Ref. 3, IA, 2nd order *KMT* |
| SMI | 500 | 1.14 | | | | | | | Ref. 4, IA |
| | | 1.23 | 1.26 | | | | | | Ref. 4, effective force |
| VPM-VDM | 400 | 1.06 | 0.94 | 0.77 | 1.07 | 1.14 | | | Ref. 32, POP |
| VPM-VDM | 334 | 1.12 | | | 1.07 | 0.89 | | | Refs. 8 and 32 POP |
| VPM-VDM | 318 | 0.98 | 0.91 | 0.83 | 0.96 | 0.94 | 0.64 | 1.24 | Table II, $\beta_{so}=\beta_c$ |
| | | | | | | | 0.50 | 0.93 | Table II, $\beta_{so}=1.5\beta_c$ |
| SCM | | 0.86 | 1.02 | 0.85 | 0.80 | 0.83 | 0.82 | 0.95 | Table V, POP-I |
| SCM | | 1.02 | 1.16 | 0.98 | 1.02 | 1.01 | 0.96 | 1.07 | Table V, fifth column |
| VPM-VDM | 200 | 0.96 | 0.95 | 0.73 | 0.95 | 0.90 | | | Ref. 32, POP |
| VPM-VDM | 155 | 0.95 | | | 0.87 | | | | Refs. 30, 31, POP |
| VPM-VDM | 135 | 0.91 | 0.77 | 0.70 | 0.99 | 0.84 | 0.43[d] | 0.20[e] | Ref. 14, POP |
| VPM-VDM | 120 | 0.75 | | | | | | | Ref. 29, POP |
| VPM-VDM | 98 | 0.92 | | | 0.78 | | | | Ref. 29, POP |
| VPM-VDM | 80 | 0.82 | | | | | | | Ref. 29, POP |
| VPM-VDM | 65 | 1.12 | | | 0.89 | | | | Ref. 28, POP[g] |
| VPM-VDM | 61 | 0.96 | 0.84 | 0.83 | 0.99 | 0.87 | 0.62 | 1.31 | Ref. 27, POP[g] |
| VPM-VDM | 35 | 1.12 | 1.18 | 0.86 | 1.00 | 0.88 | 0.68 | 1.24 | Ref. 26, POP[g] |
| $(\alpha,\alpha')$ MI | 104($T_\alpha$) | 1.19(3)[f] | | | | | | | Ref. 25, folded |
| Theory | | 0.92 | | | | | | | RPA, Ref. 37 |
| | | 1.06 | | | | | | | Particle-vib. coupling, Ref. 38 |
| | | 1.00 | 1.23 | 0.69 | 0.93 | 0.91 | 0.85 | | RPA, Ref. 39 |

[a](p,p')−(e,e') comparison unless noted. Values of $\delta_u$ given in Table II for VPM analyses. Error estimates shown in Figs. 22–26.
[b]This work unless noted.
[c]Potential given in footnote k, Table II.
[d]$\beta_{so}=1.5\beta_c$.
[e]$\beta_{so}=2.5\beta_c$.
[f]Using $B(E\lambda)=0.621e^2b^3$.
[g]Both volume and surface imaginary central terms used.

of the optical potential was calculated using free N-N amplitudes. Calculations were also done at 500 MeV using free N-N amplitudes throughout (IA) for comparison.

In both the 800 and 500 MeV SMI analyses, the parameters of the point neutron density functions were determined and then used to calculate $\tilde{M}_n/\tilde{M}_p$. These are shown in Tables VI and VII along with values obtained by other methods.

A Fourier-Bessel model independent (MI) analysis has been done by Corcalciuc, *et al.*[25] of 104 MeV $(\alpha,\alpha')$ data on the $3^-$ state of $^{208}$Pb. The validity of the folding model was assumed for the elastic and transition potentials. From their results we have calculated a value of $\tilde{M}_n/\tilde{M}_p$ which is also shown in Table VI.

## IV. VPM-VDM ANALYSIS

In this section we present the values of $\tilde{M}_n/\tilde{M}_p$ derived from proton potential deformation lengths, $\delta_U$ from these and other experiments[8,26–36,43–50] in the $T_p=35$–800 MeV energy range using the VDM. The data from other experiments were reanalyzed using a common scheme, set of $B(E\lambda)$ values, and $\bar{R}$ from Eq. (3). The $B(E\lambda)$'s used are the adopted values from Ref. 2, unless otherwise noted. The method of obtaining $\tilde{M}_n/\tilde{M}_p$ is similar to that of an earlier paper,[2] but the equations have been generalized to appropriately weight the real and imaginary parts of the nucleon-nucleon interaction, and the optical potentials, since at the lower energies they are comparable in magnitude.

A summary of the basic equations used is given here. They are derived in the Appendix. The radial part of the inelastic transition potential, $V_\lambda$, is assumed to be

$$V_\lambda=\delta_U\frac{\delta U}{\delta r}\ ,$$

where $\delta_U=\beta\bar{R}$ is the average potential deformation length, $\bar{R}$ being defined by Eq. (3), and $U$ is the central part of the POP,

$$U=(V_p+V_n)+i(W_p+W_n)\ ,$$

decomposed into neutron and proton parts. In this scheme, the contribution to the cross sections of the deformed spin-orbit term is neglected since it is generally

TABLE VII. Reduced neutron-proton matrix element ratios, $\tilde{M}_n/\tilde{M}_p$ for $^{40}$Ca and $^{58}$Ni derived by various methods.

| Nucleus | State $J^\pi$ (MeV) | Method | $T_p$ (MeV) 25 | 40 | 55 | 156 | 334 | 362 | 500 | 800 | Comments |
|---|---|---|---|---|---|---|---|---|---|---|---|
| $^{40}$Ca | $2^+$ (3.90)[a] | VPM-VDM | 0.80 | 0.83 | | | 0.76 | 0.75 | 0.98 | 1.15 | Data, Refs. 35, 36, 43, 48 and 50 |
| | | SMI | | | | | | | 0.98 | | Ref. 4, effective force |
| | $2^+$ (5.63)[b] | VPM-VDM | | | | | 0.94 | | | 1.16 | Data, Refs. 35, 36 |
| | $2^+$ (6.91)[c] | VPM-VDM | 1.09 | 1.13 | 0.97 | (1.06) | 1.01 | | | (1.36) | Data, Refs. 35, 36, 43, 44 and 49 |
| | $3^-$ (3.74)[d] | VPM-VDM | 1.01 | 0.92 | 0.94 | 0.86 | | 0.77 | 1.027 | 0.98 | Data, Refs. 36, 43, 44, 48, 49 and 50 |
| | | SMI | | | | | | | 0.78 | | Ref. 4, IA |
| | | SMI | | | | | | | 0.90 | | Ref. 4, effective force |
| | $5^-$ (4.49)[e] | VPM-VDM | 1.34 | 1.12 | 0.89 | | | 0.87 | | 1.05 | Data, Refs. 36, 43, 44 and 50 |
| | | | 40[f] | 40[g] | 178[h] | 333[i] | 500[i] | 800[j] | | | |
| $^{58}$Ni | $2^+$ (1.45) | SCM | | | | 1.19 | 1.01 | 1.17 | | | $\delta_p$ from Ref. 16 |
| | | VPM-VDM | 0.95 | 1.09 | 0.96 | 0.99 | 0.97 | 1.12 | | | |
| | $2^+$ (3.04) | VPM-VDM | | 0.90 | | 0.47 | 0.87 | 0.99 | | | $B(E\lambda)$ values |
| | $2^+$ (3.26) | VPM-VDM | | 0.92 | 1.08 | 0.95 | 0.99 | 1.04 | | | from Refs. 2 |
| | $3^-$ (4.48) | VPM-VDM | 0.87 | 0.90 | 0.69 | 0.45 | 0.73 | 0.78 | | | and 40; |
| | $4^+$ (2.46) | VPM-VDM | | 1.01 | 0.73 | 0.89 | 0.85 | 1.06 | | | $\delta_p$ values shown |
| | $4^+$ (3.62) | VPM-VDM | | 0.56 | 0.35 | 0.44 | 0.27 | 0.64 | | | in Table IV |
| | $4^+$ (4.40) | VPM-VDM | | 0.90 | | 0.67 | 0.57 | (1.44)[k] | | | |
| | $4^+$ (4.76) | VPM-VDM | | 1.07 | 0.94 | 0.84 | 0.80 | 1.00 | | | |

[a] $B(E2)=0.0103(13)e^2b^2$ adopted from values in Ref. 2 and from Refs. 41 and 42.
[b] $B(E2)=0.00084(10)e^2b^2$ adopted, references as in a above.
[c] $B(E2)=0.0075(20)e^2b^2$ adopted, references as in a above.
[d] $B(E3)=0.0180(9)e^2b^3$ adopted, references as in a above.
[e] $B(E5)=3.1(4)\times10^{-4}e^2b^5$ adopted, references as in a above.
[f] Data from Ref. 45.
[g] Data from Ref. 46.
[h] Data from Ref. 47.
[i] This work. $\tilde{M}_n\tilde{M}_p$ values tabulated for $^{58}$Ni are averages of those obtained from *SN* and *P*2 potentials (333 MeV), *SN* and *P*3 potentials (498 MeV), and from the *MK* potential (800 MeV) given in Table III. Individual values obtained using potentials listed in Table III are shown in Figs. 28 and 29.
[j] Data from Ref. 15.
[k] At 800 MeV the $4^+$ (4.40) state is poorly resolved from the $3^-$ (4.48) state.

less than $\simeq 5\%$ (except for high spin states at the lowest energies) at forward angles where theory is normalized to data. Since the deformation lengths represent displacements of the nuclear surface, we assume

$$\delta_{v_p}=\delta_{w_p}=\delta_p \text{ and } \delta_{v_n}=\delta_{w_n}=\delta_n \text{ and } \delta_p=\delta_q ,$$

where $\delta_p$, $\delta_n$, and $\delta_q$ are the proton, neutron, and charge deformation lengths and $\delta_v$, $\delta_w$ are the potential deformation lengths. We then show

$$\delta_n=\tfrac{1}{2}\{-(\alpha\delta_p)\pm[(\alpha\delta_p)^2-4C]^{1/2}\} , \tag{5}$$

and

$$C=(\tau\delta_p)^2-\delta_U^2(1+\tau^2+\alpha) . \tag{6}$$

Expressions for calculating $\tau^2$ and $\alpha$ are given in the Appendix. They involve volume integrals of the N-N $t$ matrix (taken from Ref. 17) and geometry parameters (Ref. 2). The equations reduce to the linear equations of Ref. 2 if one part (real or imaginary) of the optical potential

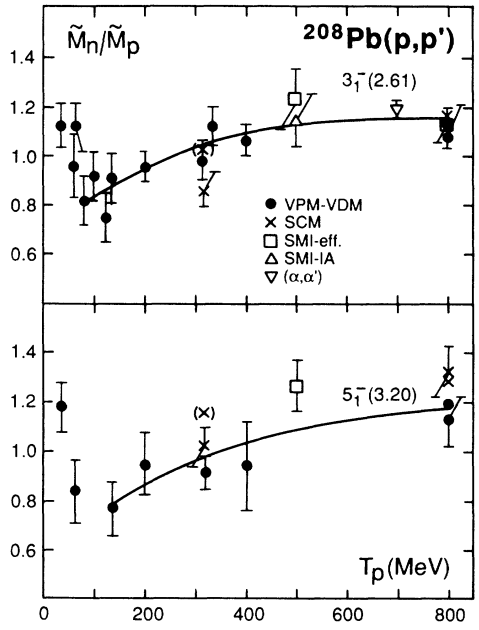


FIG. 22. Reduced neutron-proton matrix element ratios, $\tilde{M}_n/\tilde{M}_p$ for $3_1^-$ (2.61 MeV) and $5_1^-$ (3.20 MeV) states of $^{208}$Pb derived by various methods (from proton and electron scattering data, unless noted) vs proton energy. Values shown by solid circles are from the VPM-VDM ("collective form factors"), crosses are from the scaling model (SCM), open squares are from semi-model-independent analyses (SMI) using effective forces, and erect triangles from SMI analyses using the free $t$-matrix (IA). The inverted triangle is from a model independent (MI) analysis of $(\alpha,\alpha')$ data (Ref. 25) at $T_\alpha=104$ MeV and is arbitrarily plotted at $T_p=700$ MeV. The error bars shown are estimates based on uncertainties in normalizing theory to the (p,p') data and do not reflect statistical or systematic cross section errors, or errors in the (common) $B(E\lambda)$ values adopted to obtain the proton matrix elements. Parentheses indicate poor fits to the data. Numerical values are given in Table VI. The lines are drawn by eye to indicate the average energy dependence suggested by the data above 100 MeV.

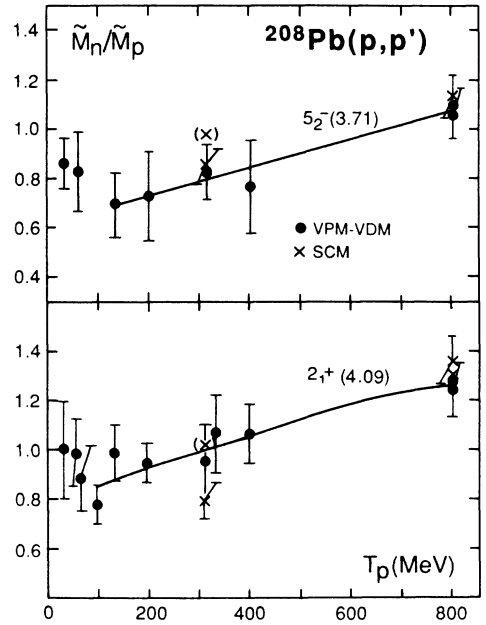


FIG. 23. Same as Fig. 22 except for $5_2^-$ (3.71 MeV) and $2_1^+$ (4.09 MeV) states of $^{208}$Pb.

dominates. The proton deformation lengths, $\delta_p=\delta_q$, and the reduced matrix element ratios are calculated using

$$\tilde{M}_i=\left[\frac{\lambda+2}{4\pi}\langle r^{\lambda-1}\rangle_i\delta_i\right] \quad i=\text{n,p or } q , \tag{7}$$

and

$$B(E\lambda)\uparrow=|Z\tilde{M}_q|^2 , \tag{8}$$

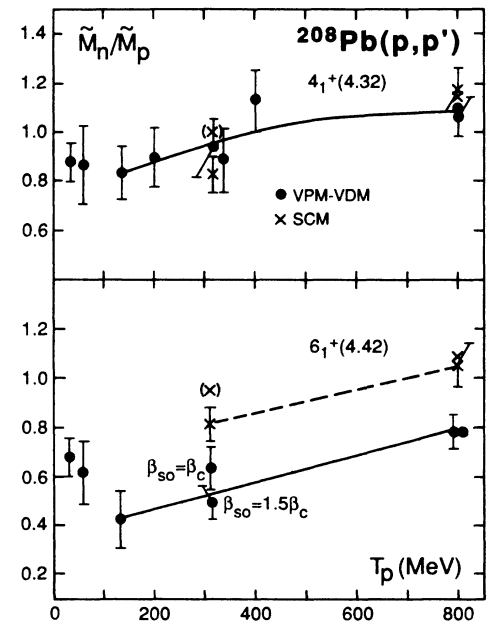


FIG. 24. The same as Fig. 22 except for the $4_1^+$ (4.32 MeV) and $6_1^+$ (4.42 MeV) states of $^{208}$Pb. The approximate energy dependence of the SCM results (crosses) is shown separately from that of the VPM-VDM.

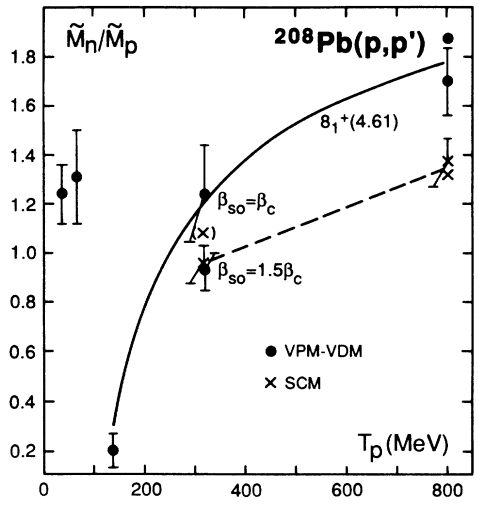


FIG. 25. The same as Fig. 22 (and 24) except for the $8^+$ (4.61 MeV) state of $^{208}$Pb.

then

$$\tilde{M}_n/\tilde{M}_p=\frac{\langle r^{\lambda-1}\rangle_n\delta_n}{\langle r^{\lambda-1}\rangle_p\delta_p}\ . \tag{9}$$

The radial moments of the ground state densities are taken from the best available electron and proton scattering analyses and are tabulated in Ref. 2.

The results for $\tilde{M}_n/\tilde{M}_p$ for the $3_1^-$, $5_1^-$, $5_2^-$, $2_1^+$, $4_1^+$, $6_1^+$, $8_1^+$ states of $^{208}$Pb, the $2_1^+$, (3.90), $2^+$ (5.63), $2^+$ (6.91), $3_1^-$, $5^-$ states of $^{40}$Ca, and eight of the low lying states of $^{58}$Ni are given in Tables VI and VII, and plotted versus proton energy in Figs. 22–29. In the figures we have shown error estimates based mainly on the uncertainty in normalizing theory to experiment to obtain deformation lengths (VPM) or scaling factors (SCM).

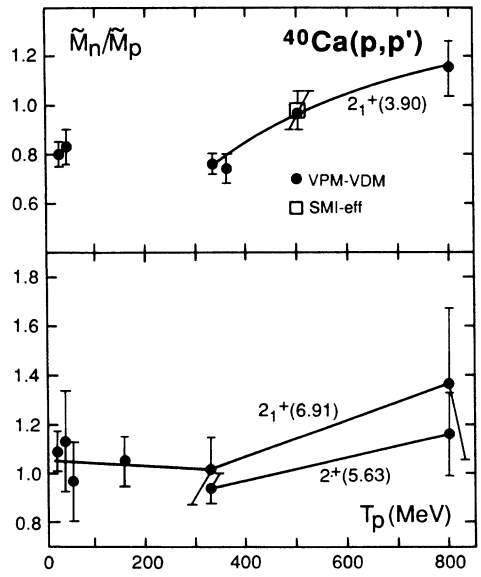


FIG. 26. The same as Fig. 22 except for the $2^+$ states of $^{40}$Ca at 3.90, 5.63, and 6.91 MeV. Numerical values and references are given in Table VII. The VPM-VDM point for the $2_1^+$ state at 500 MeV is derived from Ref. 48.

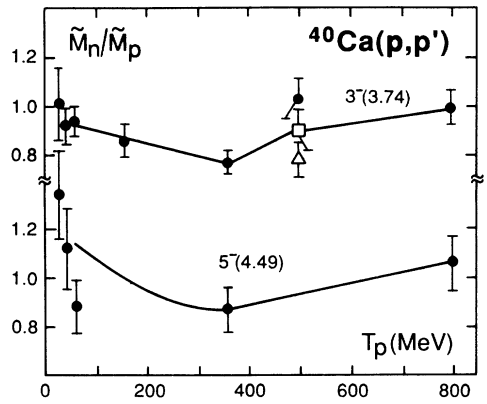


FIG. 27. The same as Fig. 22 except for the $3^-$ (3.74 MeV) and $5^-$ (4.49 MeV) states of $^{40}$Ca. Numerical values and references are given in Table VII.

This source of error usually dominates over statistical and absolute normalization errors unless the theoretical fits to data are very good. In the VPM and SCM analyses with phenomenological potentials (POP), the extracted deformation lengths ($\delta_U$) or scaling factors ($\alpha$) are somewhat insensitive to absolute data normalization uncertainties since these quantities are determined mainly by the *ratio* of inelastic to elastic cross sections. Howev-

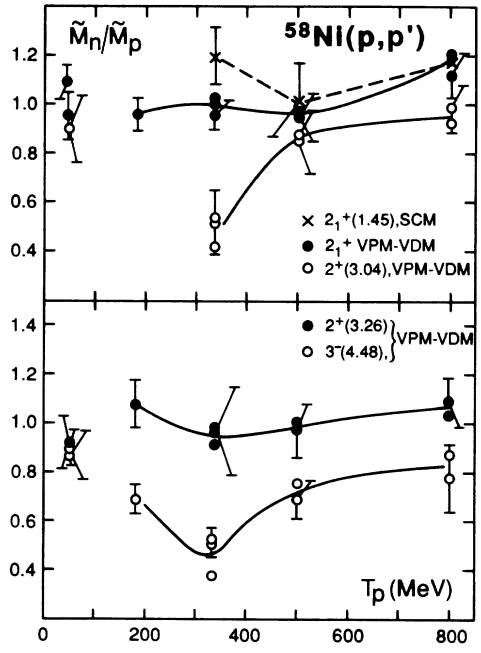


FIG. 28. Reduced neutron-proton matrix elements ratios, $\tilde{M}_n/\tilde{M}_p$ for the $2^+$ (1.45, 3.04, 3.26 MeV) and the $3^-$ (4.48 MeV) states of $^{58}$Ni derived from this analysis of proton and electron scattering data. The solid and open circles are from the VPM-VDM model, the crosses, for the $2_1^+$, (1.45 MeV) state, are from the scaling model (SCM). The individual VPM-VDM points at 333, 498, and 800 MeV are derived using the various potentials given in Table III. The errors shown are discussed in the text (Sec. IV) and the caption for Fig. 22. The lines are drawn by eye to indicate the average energy dependence suggested by the data above 100 MeV. Numerical values and references are given in Table VII.

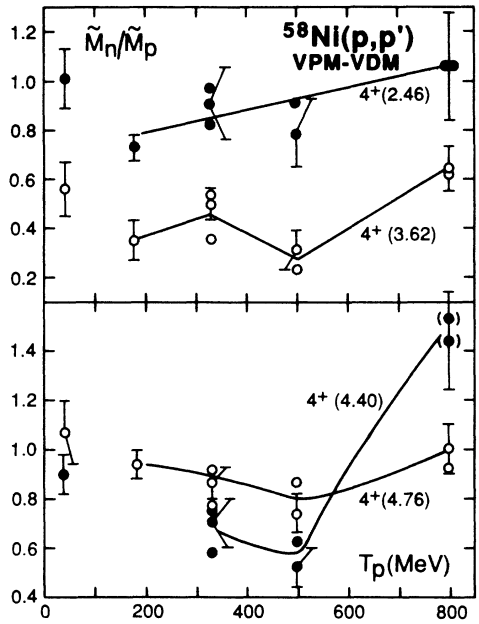


FIG. 29. The same as Fig. 28 except for the $4^+$ states in $^{58}$Ni at 2.46, 3.62, 4.40, and 4.76 MeV. The $4^+$ (4.40 MeV) is not completely resolved at 800 MeV.

er, our error estimates tend to overestimate somewhat the *relative* uncertainties in $\tilde{M}_n/\tilde{M}_p$ values obtained for the same nuclear state at different energies, since theory is usually normalized to experiment at the first maximum where the fit is generally good. We have *not* included errors due to the uncertainty in the measured $B(E\lambda)$ or proton transition density since a commom set of values was used, for a given state, at all energies in our analysis. The most important general feature of the derived $\tilde{M}_n/\tilde{M}_p$ ratios, despite some fluctuations, especially for $^{58}$Ni, is their tendency to decrease with decreasing proton energy in the range 100–500 Mev. It is interesting to note however that the low energy ($T_p < 65$ MeV) values obtained from the VPM-VDM analyses are, in general, higher than those found in the 100–400 MeV region, and are frequently close to the 800 MeV values. However, as mentioned above, the calculations at 65 MeV and below include surface absorption terms in the distorting potential which then contribute to the inelastic transition potential, while those above 100 MeV do not. The values of $\tilde{M}_n/\tilde{M}_p$ obtained at 500 MeV in the SMI analysis, using effective forces,[4] are generally close to or a bit higher than the 800 MeV values from the VPM-VDM or SCM.

The true values of $\tilde{M}_n/\tilde{M}_p$ are expected to be close to unity for $^{40}$Ca (and for the $3_1^-$ state of $^{208}$Pb). We find this at 800 MeV for the experimental $3_1^-$($^{40}$Ca and $^{208}$Pb) and $5_1^-$($^{40}$Ca) values from the VPM-VDM analysis, but those for the three $2^+$ ($^{40}$Ca) states are somewhat higher. We believe this reflects the large uncertainties in the experimental $B(E\lambda)$'s for these states (see Table VII footnotes *a*–*e*), which produces approximately the same percentage uncertainty in the derived $\tilde{M}_n/\tilde{M}_p$ values. The data thus indicate a quantitative failure of the usual DWBA or DWIA approximations in the range $\simeq$100–500 MeV.

## V. DISCUSSION AND CONCLUSIONS

We have shown that the reduced neutron to proton matrix element ratios, $\tilde{M}_n/\tilde{M}_p$ derived from intermediate energy proton inelastic scattering and electromagnetic $B(E\lambda)$ values, or change transition densities, show a tendency to decrease with decreasing proton energy, in the range 500–100 Mev. We believe this is *not* due to inadequacies in the transition potentials, or densities, since the VPM-VDM, the SCM, and to some extent the SMI analyses for $^{40}$Ca, using the DWIA, show quantitatively similar behavior.

The effect being seen is the *over prediction* of (p,p') cross sections for a given transition potential, or density, at energies below 500 MeV by an amount which seems independent of the angular momentum transfer ($L=2-8$) involved. This effect was also noted in the analysis of natural parity high spin stretched or nearly stretched particle hole states in $^{28}$Si ($5_1^-$) and $^{58}$Ni ($6_1^+$).[5]

To illustrate that the effect shown here is quantitatively the same as that noted in the Si-Ni analysis we have calculated the quantity $N_p^2=\sigma_{exp}/\sigma_{theo}$ for the (p,p')

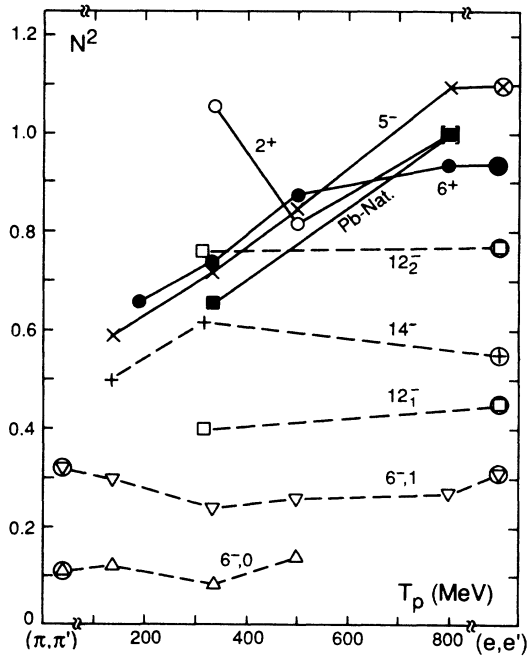


FIG. 30. Values of normalization, or "quenching" factors $N_p^2(N_e^2,N_\pi^2)=\sigma_{exp}/\sigma_{theo}$ for proton (electron, pion) inelastic excitation of natural and unnatural parity states at various energies. Points are shown for $^{58}$Si ($5_1^-$; $6^-$, $T=0,1$), $^{58}$Ni ($2_1^+$, $6_1^+$) and $^{208}$Pb (Nat., $12_{1,2}^-$, $14^-$) states. Pion and electron scattering values are circled and shown at the edges of the figure. The lines are drawn to connect the data points. The points (solid squares) labelled "Pb-Nat." are an average for the low-lying natural parity states of $^{208}$Pb given in Table V. For the $^{58}$Ni ($2_1^+$) and Pb-Nat. values we have used the scaling model (SCM) with the scaling factor taken from the 800 MeV analysis. For the remaining states, transition densities adjusted to fit electron scattering data have been used as described in the text (Sec. V) and in Refs. 5 and 6.

TABLE VIII. Ratio of experimental to theoretical cross sections, $N_p^2$, for (p,p') to natural parity states in $^{28}$Si, $^{58}$Ni and $^{208}$Pb at several energies.

| Nucleus | $J^\pi$ ($E_x$, MeV) | $T_p$ (MeV) 135 | 178 | 333/318 | 500 | 800 | $N_e^2$ (e,e') | Comments |
|---|---|---|---|---|---|---|---|---|
| $^{28}$Si | $5^-$ (9.70) | 0.59 | | 0.68–0.76 | 0.85 | 1.10 | 1.10 | Ref. 5 analysis |
| $^{58}$Ni | $2^+$ (1.45) | | | 1.06 | 0.82 | [1.0] | [1.0] | *P2,P3* potential Table III |
| | | | | 0.99 | 1.06 | [1.0] | [1.0] | *SN* potentials Table III |
| | $6^+$ (5.13) | | 0.66 | 0.74 | 0.88/1.03 | 0.94 | 0.94 | Ref. 5 analysis *P3/SN* potential Table III at 498 MeV |
| $^{208}$Pb | $3^-$ (2.61) | | | 0.71 | | [1.0] | [1.0] | POP-I, Table I, IA |
| | | | | 0.73 | | [1.0] | [1.0] | POP, GBJ force, Ref. 21 |
| | | | | 0.91 | | [1.0] | [1.0] | Folded pot, GBJ force, Ref. 21 |
| | $5^-$ (3.20) | | | 0.71 | | [1.0] | [1.0] | POP-I, Table I, IA |
| | $5^-$ (3.71) | | | 0.70 | | [1.0] | [1.0] | POP-I, Table I, IA |
| | $2^+$ (4.09) | | | 0.51 | | [1.0] | [1.0] | POP-I, Table I, IA |
| | $4^+$ (4.32) | | | 0.65 | | [1.0] | [1.0] | POP-I, Table I, IA |
| | $6^+$ (4.42) | | | 0.72 | | [1.0] | [1.0] | POP-I, Table I, IA |
| | $8^+$ (4.61) | | | 0.64 | | [1.0] | [1.0] | POP-I, Table I, IA |

data on $^{208}$Pb at 318 MeV, and the $^{58}$Ni ($2_1^+$) data at 333 and 500 MeV, using the SCM, with the scaling parameter $\alpha$ taken from the 800 MeV analyses (Tables V and VII). The results for natural parity states in $^{208}$Pb, and in $^{28}$Si and $^{58}$Ni from our earlier work are shown in Table VIII and Fig. 30.

Values of $N_p^2$ at various energies for unnatural parity stretched states in $^{28}$Si and $^{208}$Pb (Refs. 5 and 6) are also plotted in Fig. 30. These have been obtained from common transition densities adjusted to fit the $q$ dependence of both the electron and proton scattering data. It is seen that these do not show the strong energy dependence exhibited by the natural parity states, and, furthermore, the quenching factors ($N_p^2$ for protons) obtained at various proton energies are reasonably consistent with the electron (and pion) values. The excitation of the unnatural parity states does not involve the central, spin-independent parts of the N-N force which dominates in the excitation of the natural parity states. It should also be noted that the proton $N_p^2$ values obtained at $T_p = 800$ MeV for the *natural* parity states are in good agreement with the quenching factors found in electron excitation.

Since the inelastic cross sections, for the low lying natural parity states, calculated in the DWBA (VPM) or DWIA (SCM or SMI analyses) are dominated by the central, spin-independent parts of the N-N interaction, we believe that these results indicate a progressive (with decreasing energy) deficiency in this part of the assumed inelastic interaction. In general, the *elastic* cross sections have been reproduced with an optical potential whose magnitude is determined (in a microscopic model) by the very low-$q$ ($q \leq 0.2\text{fm}^{-1}$) part of the above N-N interaction, since the ground state density, in momentum space, decreases rapidly with $q$. However, the *inelastic* cross sections, even at the first maxima for low spin states, are sensitive to the higher $q(\geq 0.5\text{fm}^{-1})$ behavior of the N-N interaction. Thus, potentials or effective interactions adjusted to fit *elastic* data appear to be inadequate when used to calculate inelastic transition potentials in the 100–400 MeV region. This is the main conclusion of our work.

## APPENDIX

At 800 MeV the imaginary central potential ($W$) dominates in the VPM-VDM analysis. Thus, in the equations of Ref. 2, the various quantities are evaluated for the imaginary central part of the optical potential, or the imaginary part of the nucleon-nucleon interaction. At lower energy, the real and imaginary parts are comparable and so the equations for obtaining the neutron deformation lengths, $\delta_n$, from the potential and proton deformation lengths, $\delta_U$ and $\delta_p$, must be generalized.

As before, we decompose the optical potential $U(r)$ into target neutron and proton parts (neglecting the spin-orbit terms),

$$U = V + iW = (V_p + V_n) + i(W_p + W_n) . \quad \text{(A1)}$$

The transition potential, $V_\lambda(r)$ is then

$$V_\lambda = \delta_U [V'_p + V'_n + i(W'_p + W'_n)] , \quad \text{(A2)}$$

where the primes denote radial derivatives.

In most analyses the deformation parameter, $\beta$, is the same for all parts of the potential, resulting in different deformation lengths $\delta_v = \beta R_v$ and $\delta_w = \beta R_w$ for the real and imaginary parts of the transition potential, i.e., most DWBA calculations assume

$$V_\lambda(r) = \beta [R_v V'(r) + iR_w W'(r)] . \quad \text{(A3)}$$

If we assume the scattering amplitude scales approximately as the volume integral of the interaction potential, $J_0(V_\lambda)$, then

$$\sigma \alpha \beta^2 [R_v^2 J_0^2(V') + R_w^2 J_0^2(W')] . \quad \text{(A4)}$$

If the potential form factors are Fermi functions eg.,

$$V(r)=V\left[1+\exp\left[\frac{r-R_v}{a}\right]\right]^{-1}$$

then the volume integrals of the potential derivatives scale approximately as $VR_v^2$ and $WR_w^2$ thus

$$\sigma\alpha\beta^2[(VR_v^3)^2+(WR_w^3)^2] \tag{A5}$$

we can then define the average potential deformation in length, $\delta_v=\beta\bar{R}$ to be used in Eq. (A2) as,

$$\bar{R}=\left[\frac{(VR_v^3)^2+(WR_w^3)^2}{(VR_v^2)^2+(WR_w^2)^2}\right]^{1/2} . \tag{A6}$$

We now assume Eq. (A2) to be the usual VPM-VDM approximation to an interaction potential in which the neutron and proton deformation lengths, $\delta_n$ and $\delta_p$ appear separately, i.e.,

$$V_\lambda=\delta_p(V'_p+iW'_p)+\delta_n(V'_n+iW'_n) . \tag{A7}$$

Again using volume integrals to approximate the scaling of the scattering amplitudes and equating the cross sections from Eqs. (A2) and (A7) we obtain

$$\delta_p^2P_p^2+\delta_n^2P_n^2+2Q_{pn}\delta_p\delta_n=\delta_U^2[P_p^2+P_n^2+2Q_{pn}] , \tag{A8}$$

where $P_p^2=J_0^2(V'_p)+J_0^2(W'_p)$ ,

$$P_n^2=J_0^2(V'_n)+J_0^2(W'_n) ,$$

$$Q_{pn}=J_0(V'_p)J_0(V'_n)+J_0(W'_p)J_0(W'_n) , \tag{A9}$$

then $\delta_n=\frac{1}{2}\{-(\alpha\delta_p)\pm[(\alpha\delta_p)^2-4C]^{1/2}\}$ ,

where $\alpha=\dfrac{2Q_{pn}}{P_n^2}$, $\tau^2=P_p^2/P_n^2$ ,

and $C=(\tau\delta_p)^2-\delta_U^2(1+\tau^2+\alpha)$ .

To evaluate the quantities $P_p$, $P_n$ and $Q_{pn}$ we use folding theorems to relate the potential volume integrals to the nucleon-nucleon force and the matter densities. For a potential, $V(r)$, obtained by folding a matter density, $\rho(r')$ with a $t$ matrix, $g(|\mathbf{r}-\mathbf{r}'|)$, we have

$$J_0(V)=J_0(\rho)J_0(g)=(N \text{ or } Z)J_0(g) . \tag{A10}$$

If the density and potential shapes are given by Fermi functions, then for example, to a sufficient approximation,

$$J_0(V'_p)/J_0(V_p)=-\frac{3}{R_{v_p}} , \tag{A11}$$

and thus

$$J_0(V'_p)=-\frac{3Z}{R_{v_p}}J_0(g_{pR}) , \tag{A12}$$

where $J_0(g_{pR})$ is the volume integral of the real part of the projectile-proton interaction.

Finally, since the phenomenological Woods-Saxon potentials (POP) do not, in general, satisfy the folding Eqs. (A10) we modify Eq. (A12) by introducing normalization factors, $N_v$ and $N_w$ where, eg.,

$$N_v=\frac{J_0(V)_{\text{POP}}}{J_0(V)_{\text{FOLD}}} , \tag{A13}$$

thus we use

$$J_0(V'_p)=-\frac{3ZN_vJ_0(g_{pR})}{R_{v_p}} . \tag{A14}$$

We then assume

$$R_{v_n}/R_{v_p}=R_{w_n}/R_{w_p}=R_n/R_p , \tag{A15}$$

and

$$R_{v_n}/R_{w_n}=R_{v_p}/R_{w_p}=R_v/R_w ,$$

where $R_n$ and $R_p$ are the neutron and proton matter radii and $R_v$, $R_w$ are the POP radii.

With these assumptions, the equations for $\alpha$ and $\tau^2$ become

$$\tau^2=\left[\frac{ZR_n}{NR_p}\right]^2\frac{J_0^2(g_{pR})+GJ_0^2(g_{pI})}{J_0^2(g_{nR})+GJ_0^2(g_{nI})} , \tag{A16}$$

and $\alpha=2\dfrac{ZR_n}{NR_p}\dfrac{J_0(g_{pR})J_0(g_{nR})+GJ_0(g_{pI})J(g_{nI})}{J_0^2(g_{nR})+GJ_0^2(g_{nI})}$ ,

where $G=\left[\dfrac{N_wR_v}{N_vR_w}\right]^2$ .

The volume integrals of the $t$ matrix, $J_0(g)$ were taken from Ref. 17. The radii $R_v$ and $R_w$, and the normalizing factors, $N_v$ and $N_w$ were obtained from the POP's used by each author and Eq. (A13). For $R_n$ and $R_p$ we used the rms radii tabulated in Ref. 2.

Thus we have incorporated the differing potential ($V$ and $W$) and matter (n and p) geometries in the model. The $t$-matrix volume integrals have been used only to obtain the ratio of the neutron and proton parts of the interaction potential.

If one part of the potential (say, $W$) dominates, i.e.,

$$GJ_0^2(g_I)\gg J_0^2(g_R) ,$$

then $\alpha\simeq 2\tau=2\dfrac{ZR_n}{NR_p}\dfrac{J_0(g_{pI})}{J_0(g_{nI})}$ ,

and $\delta_n\simeq\delta_U(1+\tau)-\tau\delta_p$ , \tag{A17}

which is equivalent to Eq. (11) of Ref. 2.

In this approximation, $\tau\simeq Z/N\langle\nu\rangle$, where $\langle\nu\rangle$ is defined in Ref. 2. It should be noted that the value of $\delta_n$ extracted from Eqs. (A9) or (A17) is fairly insensitive to the values of $\tau$ and $\alpha$ unless $\delta_U$ and $\delta_p$ are very different.

*Present address: Physics Department, Rutgers University, New Brunswick, NJ 08903.
[1]See, for example, *Nuclear Structure,* edited by A. Bohr and B. Mottelson (Benjamin, Reading, MA, 1975), Vol. II, Chap. 6.
[2]M. M. Gazzaly, N. M. Hintz, G. S. Kyle, R. K. Owen, G. W. Hoffmann, M. Barlett, and G. Blanpied, Phys. Rev. C **25**, 408 (1982).
[3]L. Ray and G. W. Hoffmann, Phys. Rev. C **27**, 2133 (1983).
[4]M. L. Barlett, G. W. Hoffmann, and L. Ray, Phys. Rev. C **35**, 2185 (1987).
[5]N. M. Hintz *et al.*, Phys. Rev. C **30**, 1976 (1984).
[6]D. Cook *et al.*, Phys. Rev. C **35**, 456 (1987).
[7]Calculated from data base program SAID, R. Arndt (unpublished).
[8]F. E. Bertrand *et al.*, Phys. Rev. C **34**, 45 (1986); F. E. Bertrand, private communication.
[9]L. E. Smith, program LOAF (unpublished) (1983).
[10]W. T. Wagner, G. M. Crawley, G. R. Hammerstein, and H. McManus, Phys. Rev. C **12**, 757 (1975).
[11]D. A. Hutcheon, private communication.
[12]G. J. Pyle, Program RAROMP, University of Minnesota Informal Report No. COO-1265-64, 1964 (unpublished), modified for relativistic energies.
[13]H. V. von Geramb, in *The Interaction Between Medium Energy Nucleons in Nuclei* (Indiana Cyclotron Facility, Bloomington, Indiana), Proceedings of the Workshop on the Interactions Between Medium Energy Nucleons in Nuclei, AIP Conf. Proc. No. 97, edited by Hans-Otto Meyer (AIP, New York, 1982), p. 43, and private communication.
[14]G. S. Adams, A. D. Bacher, G. T. Emery, W. P. Jones, D. W. Miller, W. G. Love, and F. Petrovich, Phys. Lett. **91B**, 23 (1980).
[15]G. S. Kyle, *et al.*, Phys. Lett. **91B**, 353 (1980).
[16]J. Heisenberg, J. Lichtenstadt, C. N. Papanicolas, and J. S. McCarthy, Phys. Rev. C **25**, 2292 (1982); J. Heisenberg, *Advances in Nuclear Physics* (Plenum, New York, 1981), Vol. 12, p. 61.
[17]M. A. Franey and W. G. Love, Phys. Rev. C **31**, 488 (1985).
[18]K. Nakayama, S. Krewald, J. Speth, and W. G. Love, Nucl. Phys. **A431**, 419 (1984).
[19]B. Frois *et al.*, Phys. Rev. Lett. **38**, 152 (1977).
[20]G. W. Hoffmann *et al.*, Phys. Rev. C **21**, 1488 (1980).
[21]D. C. Cook, Ph.D thesis, University of Minnesota, 1985, unpublished.
[22]J. Kelly *et al.*, Phys. Lett. **169B**, 157 (1986).
[23]R. A. Arndt and D. Roper, VPI and SU Scattering Analysis Interactive Dialin Nucleon-Nucleon Program, and private communication.
[24]M. L. Barlett, W. R. Coker, G. W. Hoffmann, and L. Ray, Phys. Rev. C **29**, 1407 (1984).
[25]V. Corcalciuc, H. Rebel, R. Pesl, and H. J. Gils, J. Phys. G: Nucl. Phys. **9**, 177 (1983).
[26]W. T. Wagner, G. M. Crawley, G. R. Hammerstein, and H. McManus, Phys. Rev. C **12**, 757 (1975).
[27]A. Scott, N. P. Mathur, and F. Petrovich, Nucl. Phys. **A285**, 222 (1977).
[28]Y. Fujita *et al.*, Phys. Rev. C **32**, 425 (1985).
[29]S. Kailas, P. P. Singh, D. L. Griesel, C. C. Foster, P. Schwandt and J. Wiggins, Phys. Rev. C **29**, 2075 (1984); S. Kailas, *ibid.* **35**, 2324 (1987).
[30]V. Comparat, R. Frascaria, N. Marty, M. Morlet, and A. Willis, Nucl. Phys. **A221**, 403 (1974).
[31]N. Marty, M. Morlet, A. Willis, V. Comparat, and R. Frascaria, Nucl. Phys. **A238**, 93 (1975).
[32]D. K. McDaniels *et al.*, Phys. Rev. C **33**, 1943 (1986); D. K. McDaniels, private communication.
[33]G. W. Hoffmann *et al.*, Phys. Rev. C **21**, 1488 (1980).
[34]D. K. McDaniels *et al.*, Nucl. Phys. **A467**, 557 (1987).
[35]D. J. Horen *et al.*, Phys. Rev. C **30**, 709 (1984).
[36]G. S. Adams *et al.*, Phys. Rev. C **21**, 2485 (1980).
[37]J. Lichtenstadt, Ph.D. thesis, MIT, 1979; unpublished; J. Heisenberg, private communication.
[38]I. Hamamoto, Phys. Lett. **66B**, 410 (1977) and private communication.
[39]J. Decharge, M. Girod, D. Gogny, and B. Grammaticos, Nucl. Phys. **A358**, 203C (1981); J. Decharge, private communication.
[40]H. Blok, Ph.D thesis, Vrije Universiteit te Amsterdam, 1986, unpublished.
[41]R. Moreh, W. M. Sandefur, W. C. Sellyey, D. C. Sutton, and R. Vodhanel, Phys. Rev. C **25**, 1824 (1982).
[42]K. Seth, private communication.
[43]C. R. Gruhn, T. Y. T. Kuo, C. J. Maggiore, H. McManus, F. Petrovich, and B. M. Preedom, Phys. Rev. C **6**, 915 (1972).
[44]K. Yagi *et al.*, Phys. Lett. **10**, 186 (1964).
[45]M. P. Fricke, E. E. Gross, and A. Zucker, Phys. Rev. **163**, 1153 (1967).
[46]K. M. Thompson, Ph.D. thesis, Michigan State University, 1969, unpublished.
[47]A. Ingemarsson, T. Johansson, and G. Tibell, Nucl. Phys. **A365**, 426 (1981).
[48]K. K. Seth *et al.*, Phys. Lett. **158B**, 23 (1985).
[49]R. M. Haybron and H. McManus, Phys. Rev. **140**, B638 (1965).
[50]D. Frekers *et al.*, Phys. Rev. C **35**, 2236 (1987).